Research Square

Preprints are preliminary reports that have not undergone peer review.
They should not be considered conclusive, used to inform clinical practice,
or referenced by the media as validated information.

Efficient uncertainty quantification in FDEM inversion using an adjusted Bayesian information criterion

Zekai Deng
Institute of Geology and Geophysics
Hai Li
lihai@mail.iggcas.ac.cn

Institute of Geology and Geophysics
Ziteng Li
Institute of Geology and Geophysics

Research Article

Keywords: frequency-domain electromagnetics, effective degrees of freedom, Bayesian information criterion, model-dimension uncertainty, model averaging, uncertainty quantification

Posted Date: November 4th, 2026

DOI: https://doi.org/10.21203/rs.3.rs-11361769/v1

License: This work is licensed under a Creative Commons Attribution 4.0 International License.
Read Full License

Additional Declarations: No competing interests reported.

Efficient uncertainty quantification in FDEM inversion using an adjusted Bayesian information criterion

Zekai Deng[1], Hai Li[1,*], Ziteng Li[1]

[1] Institute of Geology and Geophysics, Chinese Academy of Sciences, Beijing 100029, China

* Corresponding author: Hai Li. E-mail: lihai@mail.iggcas.ac.cn

Abstract

Frequency-domain electromagnetic (FDEM) inversion is non-unique. The resulting inversion represents only one preferred solution under the chosen parameterization and regularization. Bayesian approaches characterize such uncertainty but often require millions of forward evaluations. This study develops a framework for layer-count assessment and model-averaged uncertainty quantification using an effective-degrees-of-freedom-adjusted Bayesian information criterion (EDF-BIC). EDF-BIC replaces the nominal parameter count with the effective degrees of freedom so that the penalty reflects the data-fitting flexibility retained after regularization. Criterion differences among evaluated candidate layer counts are converted into relative-support weights. Layer-count model averaging (LCMA), combined with a Laplace approximation, propagates candidate-conditional parameter uncertainty and uncertainty among layer counts into the resistivity structure. For the five-layer U05 model, the EDF adjustment increased the weighted mean layer count from 4.06 to 5.15 and reduced the low-layer-count preference of nominal BIC. In the G02 and G05 experiments, EDF-BIC support varied spatially near layer pinch-outs, disappearing layers, and interface variations, while between-model uncertainty was concentrated in transition zones. Across 50 noise realizations with the candidate sets, error model, and regularization fixed, mean empirical coverage of the P10–P90 intervals was 87.57% for G02 and 83.66% for G05. Application to the Yemaquan L52 and L53 field data recovered consistent principal electrical structures, whereas interface positions and geometries were more sensitive to layer-count choice. EDF calculation and uncertainty analysis added less than 1% to candidate-inversion time. The framework provides a computationally tractable approach to layer-count assessment and uncertainty propagation.

Keywords frequency-domain electromagnetics; effective degrees of freedom; Bayesian information criterion; model-dimension uncertainty; model averaging; uncertainty quantification

1 Introduction

Frequency-domain electromagnetic (FDEM) methods constrain subsurface electrical structure using electromagnetic responses measured at multiple frequencies and have been widely applied in mineral exploration and environmental and hydrogeological investigations (Guo et al., 2020; Di et al., 2020). Like most geophysical inverse problems, FDEM inversion is inherently non-unique: different resistivities, layer thicknesses, and model parameterizations can produce similar observations. Regularization stabilizes the inversion through smoothing, prior information, or spatial constraints and yields an interpretable preferred

model (Constable et al., 1987; Farquharson and Oldenburg, 1998). Conventional deterministic inversion, however, generally requires the parameterization to be specified in advance. For the layered-earth models considered here, model dimension is represented by the layer count K and is distinct from the nominal parameter count used in an information-criterion penalty. The resulting inversion represents only one preferred solution under the chosen parameterization and regularization. When several layer counts explain the observations within the data uncertainties, a single preferred model does not represent uncertainty arising from the choice of layer count and may overstate confidence in local interfaces and fine-scale structure.

Uncertainty quantification (UQ) provides a fuller characterization of the non-uniqueness of FDEM inversion and the plausible range of inversion results. Bayesian inversion describes model parameters probabilistically through the posterior distribution, providing information such as parameter correlations and credible intervals. Trans-dimensional Bayesian methods additionally treat model dimension as an unknown. Minsley (2011) developed a trans-dimensional Bayesian Markov chain Monte Carlo (MCMC) method for FDEM data, and Bayesian and other probabilistic UQ methods have since been applied to a range of electromagnetic inverse problems (Ray and Key, 2012; Blatter et al., 2018, 2022a,b; Xiang et al., 2018; Liu et al., 2025). Although these approaches can provide comprehensive uncertainty estimates, exploration of a high-dimensional, nonlinear model space can require millions of forward evaluations and is computationally demanding (Ray and Key, 2012; Blatter et al., 2018). A complementary UQ method is therefore needed that avoids full posterior sampling, integrates directly with conventional deterministic inversion, and approximates both parameter and model-dimension uncertainty at lower computational cost.

Information criteria offer another means of comparing a finite set of candidate models. Criteria such as the Akaike information criterion (AIC) and the Bayesian information criterion (BIC) balance data fit against model complexity and have a well-established theoretical basis in statistical model selection and multimodel inference (Schwarz, 1978; Buckland et al., 1997; Burnham and Anderson, 2004). In electromagnetic inversion, information criteria have also been used to select regularization parameters and models. Mitsuhata et al. (2002), for example, used the Akaike Bayesian information criterion (ABIC) to balance data fit and smoothness constraints in the inversion of frequency-domain controlled-source electromagnetic (CSEM) data from a grounded-wire source. Gehrmann et al. (2016) used BIC to compare marine CSEM models with different layer counts and then performed fixed-dimensional Bayesian uncertainty analysis for the selected model. These studies demonstrate that information criteria can support model assessment in electromagnetic inversion with modest additional computation. Existing applications, however, have primarily sought a single preferred model; relative support among candidate models and the associated model uncertainty have rarely been propagated into the final inversion result. Quantifying relative support among a finite set of candidate layer counts and propagating this uncertainty through model averaging therefore remain insufficiently explored in FDEM inversion.

A further issue arises when standard BIC is applied directly to regularized FDEM inversion: model complexity must be measured appropriately. BIC commonly measures complexity by the total number of

model parameters, hereafter termed the nominal parameter count. Regularization, parameter correlation, data sensitivity, and parameter bounds all limit the extent to which individual parameters contribute to fitting the data. Consequently, the nominal parameter count does not directly reflect the effective data-fitting flexibility retained after regularization. In studies of penalized smoothing, effective degrees of freedom, and generalized information criteria, the trace of the data-space hat or influence matrix has been used to quantify the fitting degrees of freedom effectively retained by a regularized model (Craven and Wahba, 1979; MacKay, 1992; Konishi and Kitagawa, 1996; Ye, 1998). Replacing the nominal parameter count with the effective degrees of freedom may therefore provide a BIC complexity term that more closely reflects the effective model complexity retained after regularization.

This study develops an effective-degrees-of-freedom-adjusted BIC framework for layer-count assessment and model-averaged uncertainty quantification in FDEM inversion. The framework has three main components. First, the nominal parameter count is replaced by the effective degrees of freedom to formulate EDF-BIC and better represent effective model complexity under regularization. Second, EDF-BIC differences among candidate layer counts are converted into model weights, and LCMA combines multiple data-supported candidates while retaining their relative support. Third, within this finite-candidate framework, a Laplace approximation based on the Gauss-Newton Hessian is combined with model averaging to propagate both parameter uncertainty conditional on a fixed layer count and uncertainty among layer counts. An EDF-BIC stopping rule and reuse of the Jacobian and Hessian limit the additional computational cost. U05 is used to compare layer-count assessment by nominal BIC and EDF-BIC; G02 and G05 evaluate model support, model averaging, and the decomposition of within- and between-model uncertainty; and 50 repeated-noise experiments assess the repeatability and empirical coverage of model recovery and UQ. The framework is then applied to field data from lines L52 and L53 at Yemaquan.

2 Methods

The proposed workflow builds on conventional regularized FDEM inversion. After candidate models with different layer counts have been inverted, EDF-BIC is used to assess the candidate layer counts and calculate model weights. LCMA then combines the supported candidates, and the model-averaged result incorporates both parameter uncertainty conditional on a fixed layer count and uncertainty among layer counts. Candidate layer counts are expanded sequentially and terminated using an adaptive 2% stopping criterion (Fig. 1).

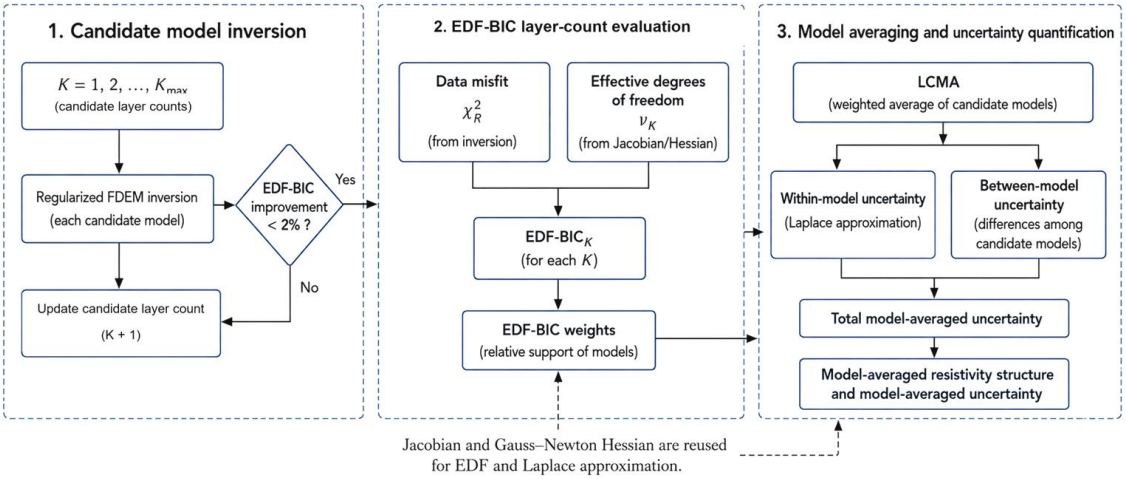


Fig. 1 Workflow of the proposed methodology

2.1 FDEM data inversion

Forward calculations and inversions are performed using layered-earth models. For a specified source, receiver position, and frequency, the open-source code empymod is used to calculate the electric field E_x and magnetic field H_y (Werthmüller, 2017). The finite-length grounded-wire source is discretized into 21 integration points. The inversion fits the complex response E_x/H_y, with the real and imaginary components weighted by their respective data uncertainties and inverted jointly. Here, E_x/H_y denotes the electric-to-magnetic field ratio for a finite source and is not interpreted as a plane-wave magnetotelluric impedance.

For the layered-earth parameterizations considered here, K denotes the number of layers in a candidate model and is therefore termed the candidate layer count. For station i and candidate layer count K, the model comprises the resistivity of each layer and the thicknesses of the finite layers, represented using a logarithmic parameterization:

$$\mathbf{m}_i^{(K)} = \left[\ln\rho_{i,1}, \ldots, \ln\rho_{i,K}, \ln h_{i,1}, \ldots, \ln h_{i,K-1}\right]^{\mathrm{T}}, \tag{1}$$

A K-layer model therefore contains $2K - 1$ nominal parameters at each station.

The residual between the observations and the forward response is

$$\mathbf{r}_{\mathrm{d},K}(\mathbf{m}_K) = \mathbf{W}_{\mathrm{d}}[\mathbf{d}_{\mathrm{obs}} - F_K(\mathbf{m}_K)], \tag{2}$$

where F_K is the FDEM forward operator for a K-layer model, and $\mathbf{W}_{\mathrm{d}}$ is constructed from the standard deviations of the real and imaginary components of the complex response.

Each candidate model is obtained by regularized nonlinear least-squares inversion:

$$\Phi_K(\mathbf{m}_K) = \|\mathbf{r}_{\mathrm{d},K}\|_2^2 + \|\mathbf{r}_{\mathrm{r},K}\|_2^2, \tag{3}$$

where $\mathbf{r}_{\mathrm{r},K}$ is the model-regularization residual. Vertically, variations in log resistivity and log layer thickness are constrained between adjacent layers. Laterally constrained inversion (LCI) imposes constraints between adjacent stations along each profile to improve inversion stability and structural continuity (Auken and Christiansen, 2004; Auken et al., 2005; Viezzoli et al., 2008).

The bound-constrained inversion uses the trust-region reflective (TRF) nonlinear least-squares algorithm, with the sparse linear least-squares subproblems solved using the least-squares minimal residual (LSMR) algorithm (Branch et al., 1999; Fong and Saunders, 2011). All candidate layer counts use the same data-error model and regularization parameters, so differences among candidates arise primarily from changes in layer count.

2.2 Bayesian information criterion adjusted for effective degrees of freedom

For each candidate layer count K, the weighted residual sum of squares χ^2_{K} is calculated at the final regularized solution and used as the BIC data-misfit term. BIC combines this term with a model-complexity penalty to compare candidate layer counts. The complexity term is modified by replacing the nominal parameter count with the effective degrees of freedom.

Here, the data-fitting degrees of freedom represent the number of effective parameter directions that can independently contribute to fitting the data, given the data sensitivities and regularization constraints. In the idealized absence of appreciable regularization and parameter correlation, this quantity can approach the nominal parameter count. Under the combined effects of regularization, parameter correlation, and limited data sensitivity, however, the retained degrees of freedom are generally smaller.

(1) Bayesian information criterion

For independent Gaussian errors, and after omitting constants shared by all candidate models, the conventional BIC can be written as (Schwarz, 1978)

$$\mathrm{BIC}_K = \chi^2_K + p_K \ln N, \tag{4}$$

where χ^2_{K} is the weighted residual sum of squares for the candidate model, N is the total number of real-valued data used in the inversion, and $\mathrm{p_K}$ is the nominal parameter count. For a K -layer model containing Ns stations, $\mathrm{p_K} = \mathrm{N_s}(2\mathrm{K}-1)$. The conventional BIC based directly on the nominal parameter count is hereafter termed nominal BIC.

BIC penalizes model complexity through $p_K \ln N$. A candidate with more layers is supported only when the improvement in data fit resulting from the additional parameters outweighs the corresponding increase in the penalty. In regularized FDEM inversion, an added parameter may be constrained by regularization, parameter correlation, or limited data sensitivity and therefore may not contribute a complete and independent degree of freedom to the fit. Direct use of the nominal parameter count may consequently overpenalize candidates with more layers.

(2) Effective degrees of freedom

To characterize the data-fitting degrees of freedom retained after regularization, effective degrees of freedom are defined (Craven and Wahba, 1979; MacKay, 1992; Konishi and Kitagawa, 1996; Ye, 1998). For candidate layer count K, the Jacobians of the data and regularization residuals with respect to the model parameters, evaluated at the final inversion model, are denoted by $\mathbf{J}_{\mathrm{d},K}$ and $\mathbf{J}_{\mathrm{r},K}$, respectively. The corresponding Gauss-Newton approximation to the Hessian is

$$\mathbf{H}_K = \mathbf{J}^{\mathrm{T}}_{\mathrm{d},K}\mathbf{J}_{\mathrm{d},K} + \mathbf{J}^{\mathrm{T}}_{\mathrm{r},K}\mathbf{J}_{\mathrm{r},K}, \tag{5}$$

The data-space influence matrix is then defined as

$$\mathbf{S}_K = \mathbf{J}_{\mathrm{d},K}\mathbf{H}_K^{-1}\mathbf{J}_{\mathrm{d},K}^{\mathrm{T}}, \tag{6}$$

and its trace defines the effective degrees of freedom of the candidate model:

$$\nu_K = \mathrm{tr}(\mathbf{S}_K). \tag{7}$$

The effective degrees of freedom quantify the data-fitting flexibility retained after accounting jointly for data sensitivity and regularization. They distinguish the nominal number of model parameters from the effective data-fitting flexibility retained by the regularized solution. Parameters at their lower or upper bounds are excluded, and EDF is calculated in the subspace of the remaining free parameters. Because EDF is based on a Gauss-Newton linearization at the final regularized solution, it describes local rather than global fitting flexibility in the nonlinear model space.

Because the influence matrix is defined in the data space of the entire profile, the diagonal elements can be summed over the data block associated with station i to obtain that station's contribution to the total EDF:

$$\nu_{i,K} = \sum_{j\in\mathcal{I}_i}[\mathbf{S}_K]_{jj}, \qquad \nu_K = \sum_{i=1}^{N_s}\nu_{i,K}, \tag{8}$$

where $\mathcal{I}_i$ is the index set of real-valued data associated with station i. This decomposition preserves consistency between station-scale model assessment and the profile-wide EDF and avoids constructing a separate Hessian for every station.

(3) EDF-adjusted BIC

The formulation replaces the nominal parameter count p_K in conventional BIC with the effective degrees of freedom ν_K and defines

$$\mathrm{EDF-BIC}_K = \chi_K^2 + \nu_K \ln N. \tag{9}$$

EDF-BIC retains the BIC trade-off between data fit and model complexity but replaces the nominal parameter count in the complexity penalty with EDF. A candidate with more layers is supported only when its improvement in data fit offsets the penalty associated with the increase in effective degrees of freedom.

EDF-BIC is also used to control expansion of the candidate layer counts. Candidates are inverted sequentially from lower to higher layer counts. The relative improvement in EDF-BIC between adjacent candidates is defined as

$$R_K = \frac{\mathrm{EDF\text{-}BIC}_{K-1} - \mathrm{EDF\text{-}BIC}_K}{|\mathrm{EDF\text{-}BIC}_{K-1}|} \times 100\%. \tag{10}$$

When $R_K < 2\%$, candidate K remains in the evaluated set, but candidate K + 1 is not evaluated. This adaptive stopping rule avoids evaluating models with progressively more layers once EDF-BIC no longer improves appreciably.

2.3 EDF-BIC model support and LCMA

Layer-count model averaging (LCMA) combines multiple supported candidate models. Because data sensitivity and structural complexity vary along a profile, the profile-wide EDF-BIC is first used to delimit the range of candidate layer counts. The relative support for those candidates is then evaluated at each station using the station's data residual and EDF contribution. For station i,

$$\mathrm{EDF-BIC}_{i,K} = \chi_{i,K}^2 + \nu_{i,K}\ln N_i, \tag{11}$$

where $\chi^2_{i,K}$ is the station-level weighted residual sum of squares, N_i is the number of real-valued data fitted at the station, and $\nu_{i,K}$ is the station's contribution to EDF. For a given station, the minimum EDF-BIC among all evaluated candidate layer counts is used as the reference:

$$\Delta_{i,K} = \text{EDF-BIC}_{i,K} - \min_j\left(\text{EDF-BIC}_{i,j}\right), \tag{12}$$

Because the profile inversion includes lateral constraints between stations, the station-scale EDF-BIC (EDF-BIC$_{i,K}$) is not obtained from an independent inversion of each station. Instead, it combines the station's data residual with the EDF contribution of the corresponding data block in the profile-wide influence matrix. It is used to characterize spatial variations in relative support among layer counts and to calculate the LCMA weights.

The EDF-BIC weights are then defined as

$$w_{i,K} = \frac{\exp(-\Delta_{i,K}/2)}{\sum_j \exp(-\Delta_{i,j}/2)}, \tag{13}$$

where $w_{i,K}$ quantifies the relative support for candidate layer count K within the finite evaluated set; the weights sum to one over all candidates. These weights are not interpreted as exact posterior model probabilities. For visualization, the spatial variation in support is summarized by the EDF-BIC-weighted mean candidate layer count:

$$E_i[K] = \sum_K K\ w_{i,K}. \tag{14}$$

When several candidate layer counts receive non-negligible support, retaining only a single preferred model makes all subsequent inference conditional on that model. Model averaging instead preserves differences in support among the candidates (Hoeting et al., 1999; Burnham and Anderson, 2004). LCMA therefore uses all evaluated candidates and their EDF-BIC weights.

Candidate models with different layer counts contain different numbers and positions of interfaces and cannot be averaged parameter by parameter. Each candidate is therefore mapped to a common depth grid, defined as a fixed set of depth samples shared by all candidates. The natural-log parameters used in inversion are converted to log10 resistivity before the mapped models are averaged in $\log_{10}\rho$ space using the EDF-BIC weights. If $\ell_{i,K}(z)$ denotes the log resistivity of candidate layer count K at station i and depth z, the LCMA model is

$$\overline{\ell}_i(z) = \sum_K w_{i,K}\ \ell_{i,K}(z). \tag{15}$$

After averaging, the mean log resistivity is converted back to resistivity. Because FDEM forward responses are nonlinear, the response of the model-averaged resistivity structure is calculated separately from the model-averaged predicted response. The latter is obtained by weighting the predicted response of each candidate model by its corresponding EDF-BIC weight and is used for the data-fit evaluations reported below.

2.4 Model-averaged uncertainty quantification

LCMA provides a weighted-average resistivity structure from multiple supported candidates, but the mean alone does not describe the magnitude or source of uncertainty. Using the law of total variance, total

model-averaged variance is decomposed into within- and between-model components. Within-model uncertainty reflects uncertainty in resistivity, layer thickness, and interface position conditional on a specified layer count. Between-model uncertainty represents differences among the mean resistivity structures obtained for the supported layer counts.

For a fixed candidate layer count K, a Laplace approximation is used (Tierney and Kadane, 1986) and the parameter covariance is approximated using the Gauss-Newton Hessian at the final inversion model:

$$\mathbf{C}_K \approx s_K^2 \mathbf{H}_K^{-1}, \tag{16}$$

where the covariance scaling factor is the EDF-based reduced chi-square:

$$s_K^2 = \frac{\chi_K^2}{(N-\nu_K)}, \tag{17}$$

where χ_K^2 is the candidate model's weighted residual sum of squares, N is the total number of real-valued data, and ν_K is its effective degrees of freedom. Joint Laplace samples are then drawn in the free-parameter subspace and embedded back into the full parameter space. The analysis uses 200 joint samples for each candidate layer count and imposes the same parameter bounds as in the inversion. To prevent weakly constrained directions from producing excessively large, physically implausible variances under the local Gaussian approximation, the current implementation caps the conditional standard deviations of $\log_{10}\rho$ and $\log_{10}h$ at 0.25 and 0.15, respectively. Covariances obtained in the natural-log parameterization are converted to log10 units before these caps are applied.

Samples from each candidate model are mapped to the same common depth grid used for LCMA. The law of total variance gives the following within- and between-model components (Draper, 1995):

$$V_{\mathrm{within},i}(z) = \sum_K w_{i,K}\, V_{i,K}(z), \tag{18}$$

$$V_{\mathrm{between},i}(z) = \sum_K w_{i,K} \left[\mu_{i,K}(z) - \overline{\mu}_i(z)\right]^2, \tag{19}$$

$$V_{\mathrm{total},i}(z) = V_{\mathrm{within},i}(z) + V_{\mathrm{between},i}(z). \tag{20}$$

The sum of these two components gives the total model-averaged variance. The decomposition distinguishes uncertainty caused primarily by limited parameter resolution within a fixed model from uncertainty caused by different structural interpretations among candidate layer counts. Samples from the candidate models are combined into a weighted mixture distribution using their EDF-BIC weights, from which P_{10}, P_{50}, P_{90}, and the P_{90}–P_{10} interval width are calculated. To ensure consistent statistics across candidates, the LCMA mean, within- and between-model variances, and weighted quantiles are all calculated in log10-resistivity space. P10, P50, and P90 are converted back to resistivity for presentation, whereas interval width is reported as log10(P90) − log10(P10).

2.5 Numerical implementation and computational-cost metrics

Because the workflow evaluates multiple candidate models sequentially, computational efficiency is important in practice. Candidates are inverted in order of increasing layer count. For each candidate with an additional layer, the starting model is generated by deterministically splitting one layer in the final model of the preceding candidate, thereby reducing redundant optimization between adjacent layer counts.

The maximum number of function evaluations is 40 per candidate, and data Jacobians are calculated by finite differences. Together with the adaptive EDF-BIC stopping rule, these settings limit the cost associated with evaluating candidates with more layers.

Both EDF and candidate-conditional uncertainty estimates are calculated from the candidate inversion results. The Jacobian and Gauss-Newton Hessian at the final solution are reused for EDF and the Laplace approximation, so neither calculation requires additional nonlinear inversion.

To reduce the influence of computer hardware on comparisons based on wall-clock time, the analysis also records the number of stationwise FDEM forward evaluations. One stationwise FDEM forward evaluation is defined as a complete calculation of the complex E_x/H_y response at all frequencies included in the inversion for a specified station and its current layered-model parameters. A K-layer model has $2K-1$ parameters per station, so the approximate number of stationwise forward evaluations for a candidate model is

$$N_{\mathrm{F},K} \approx N_{\mathrm{s}}\left[n_{\mathrm{fev},K} + (2K-1)n_{\mathrm{jev},K}\right], \tag{21}$$

where n_{fev} and n_{jev} are the numbers of function evaluations and Jacobian evaluations, respectively, recorded by TRF. Equation (21) is used only as a cost-scale estimate because the solver may make additional function calls. All forward-evaluation counts reported below are taken directly from the program logs. Table 1 summarizes the principal numerical settings used for candidate inversion, EDF calculation, and fixed-candidate uncertainty estimation.

Table 1. Principal numerical settings for candidate-model inversion and fixed-candidate uncertainty estimation.

Setting	Symbol or implementation parameter	Value
Vertical regularization strength	λ_{v}	1.0
Relative regularization weight for log layer thickness	η	1.0
Lateral-constraint strength	λ_{x}	104
Depth-decay scale of lateral constraints	L_{x}	900 m
Smoothing-transition width on the common depth profile	smooth transition	30 m
Resistivity bounds	ρ	1-10,000 Ω·m
Finite-layer thickness bounds	h	10-1000 m
Adaptive stopping threshold for EDF-BIC candidate layer counts	ε_K	2%
Maximum number of nonlinear function evaluations	$n_{\mathrm{fev,max}}$	40 (per candidate K)
TRF convergence tolerances	ftol/xtol/gtol	$10^{-6}/10^{-5}/10^{-5}$
Finite-difference step for $\mathbf{ln}\boldsymbol{h}$ and $\mathbf{ln}\boldsymbol{\rho}$	δ	10^{-4}
Numerical jitter factor for the EDF Hessian	ε	10^{-8}
Maximum condition number for pseudoinverse fallback	$\kappa_{\max}$	10^{10}
Number of joint Laplace samples	N_{samp}	200 (per candidate K)
Maximum conditional standard deviation of $\mathbf{log_{10}}\boldsymbol{\rho}$	$\sigma_{\log_{10}\rho,\max}$	0.25
Maximum conditional standard deviation of $\mathbf{log_{10}}\boldsymbol{h}$	$\sigma_{\log_{10}h,\max}$	0.15

3 Synthetic experiments and method validation

The synthetic experiments address distinct validation objectives. U05 (Fig. 2a) tests how the EDF adjustment affects the BIC complexity measure and layer-count assessment. G02 (Fig. 2b) and G05 (Fig. 2c) test candidate-layer-count expansion, station-scale model support, and structural recovery by LCMA.

The within- and between-model variance decomposition is used to examine different sources of uncertainty, and repeated-noise experiments evaluate the repeatability and empirical coverage of model recovery and model-averaged UQ.

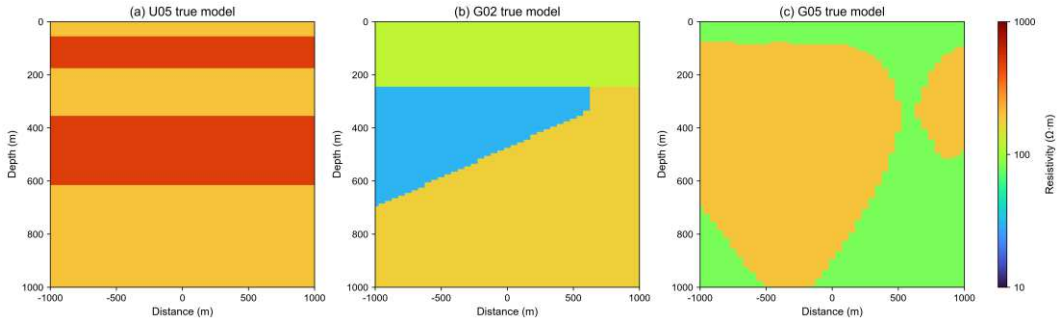


Fig. 2 True models for the three synthetic experiments. (a) Laterally uniform five-layer model U05. (b) Model G02, in which the intermediate conductive layer progressively thins and ultimately pinches out. (c) Model G05, which includes undulating interfaces and the disappearance of an intermediate resistive layer

3.1 Synthetic models and validation objectives

U05 is a laterally uniform five-layer model with layer resistivities of 200, 500, 200, 500, and 200 Ω·m and interface depths of 60, 180, 360, and 620 m. To isolate the effect of the complexity measure on layer-count assessment, all candidates with K=1–6 are evaluated without adaptive stopping. Nominal BIC and EDF-BIC are therefore compared using exactly the same candidate inversion results, data residuals, and regularization settings. Relative Gaussian noise of 5% is added to the observations, with no additional model-error term.

G02 and G05 are used to evaluate relative support among candidate layer counts, LCMA, and model-averaged uncertainty. In G02, an intermediate conductive layer progressively thins and ultimately pinches out, producing a local transition from a three-layer to a two-layer structure. G05 contains stronger interface relief and the disappearance of an intermediate resistive layer, leading to different degrees of support for one-, two-, and three-layer models along the profile. Both models use laterally varying 1D layered parameterizations to simulate variations in layer thickness and interface position. G02 and G05 each contain 41 stations and 30 logarithmically spaced frequencies from 0.25 to 5120 Hz. Relative Gaussian noise of 5% is added to the synthetic observations. A separate 3% relative model-error term is included in the inversion weights and combined in quadrature with the observational-noise standard deviation. The maximum candidate layer count is K_{max}=8.

3.2 Comparison of model dimension assessment by nominal BIC and EDF-BIC

Using the common setup described in Section 3.1, nominal BIC and EDF-BIC are compared. The two approaches differ only in their complexity measure (Fig. 3).

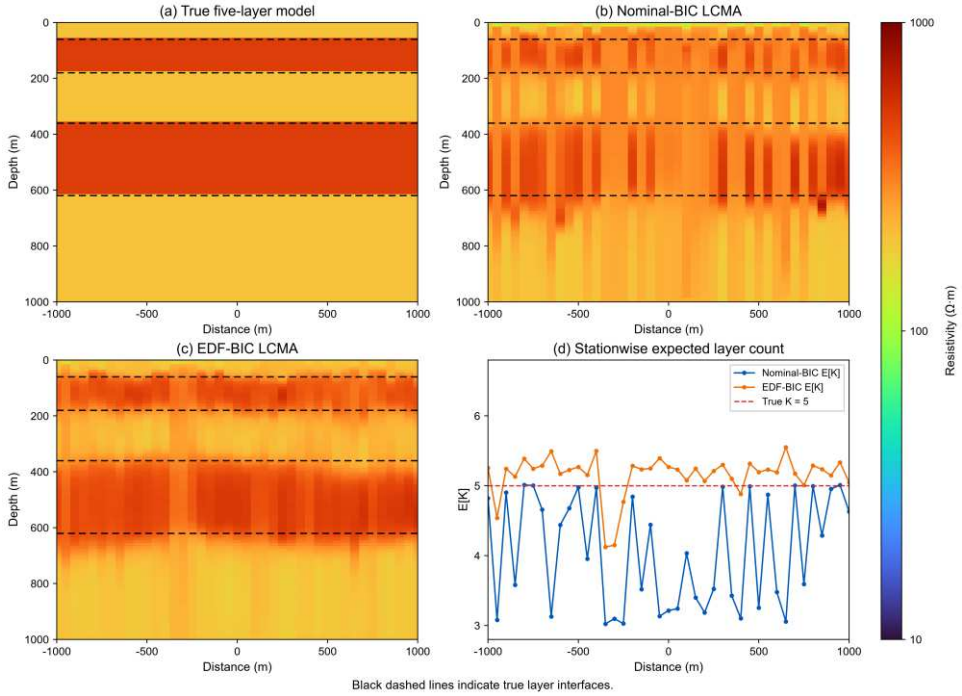


Fig. 3 Comparison of layer-count assessment by nominal BIC and EDF-BIC for the five-layer U05 reference model. (a) True U05 model. (b) Model recovered using nominal BIC. (c) Model recovered using EDF-BIC. (d) Weighted mean candidate layer counts under nominal BIC and EDF-BIC

For U05, nominal BIC shows a pronounced preference for low layer counts. The profile-averaged, nominal-BIC-weighted mean candidate layer count is 4.06 under nominal BIC, with a mean absolute deviation of 0.94 from the true five-layer configuration (Fig. 3b and 3d). After the EDF adjustment, the corresponding weighted mean increases to 5.15 (Fig. 3c and 3d), and the mean absolute deviation decreases to 0.28. Model support therefore shifts markedly toward the true five-layer configuration, consistent with EDF reducing the excessive complexity penalty produced by nominal parameter counting. EDF-BIC does not concentrate all support on a single layer count, however, but retains support for adjacent candidates. This residual spread reflects the non-uniqueness of layer count under finite data resolution. The EDF adjustment thus reduces the low-layer-count preference of nominal BIC in this regularized five-layer experiment and provides the basis for subsequent EDF-BIC weighting and LCMA.

3.3 From selecting a single dimension to quantifying relative model support

Before relative support among candidate layer counts is examined, the candidates are verified to provide reasonable fits to the observations. For both G02 and G05, the normalized root-mean-square misfit (nRMS) is near or below one at most stations (Fig. 4a and 4d). At the representative stations shown in Fig. 4b, 4c, 4e, and 4f, the predicted amplitudes and phases reproduce the principal frequency-dependent features of the observations. Subsequent changes in EDF-BIC therefore assess whether the improvement in fit obtained by increasing layer count offsets the associated increase in complexity, rather than reflecting systematic candidate-model misfit.

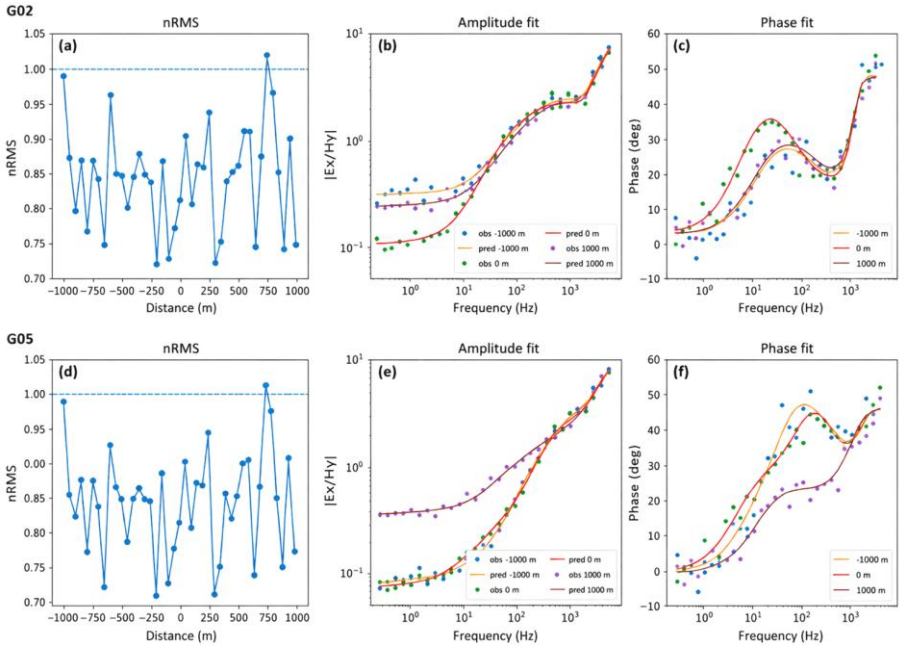


Fig. 4 Data fits for G02 and G05. (a-c) nRMS, amplitude, and phase fits for G02. (d-f) Corresponding results for G05

When the candidate layer count is increased from K=3 to K=4, nRMS decreases for both G02 and G05, but EDF-BIC increases. For G02, nRMS decreases from 0.83820 to 0.83304 while EDF-BIC increases from 2970.11 to 3072.27. For G05, nRMS decreases from 0.83835 to 0.83088 while EDF-BIC increases from 2953.74 to 3130.00. Thus, the improvement in data fit provided by the additional layer is insufficient to offset the complexity penalty associated with the increase in EDF. Under the 2% adaptive stopping criterion, expansion stops after completion of K=4 for both models. The evaluated candidate layer-count range is therefore K=1–4, below the prescribed maximum K_{max}=8.

Table 2. Candidate-layer-count expansion and effective-degrees-of-freedom statistics for G02 and G05.

Model	K	nRMS	p_K	EDF ν_K	EDF-BIC	R_K
G02	3	0.83820	205	157.23	2970.11	—
G02	4	0.83304	287	173.11	3072.27	−3.44%
G05	3	0.83835	205	154.93	2953.74	—
G05	4	0.83088	287	181.54	3130.00	−5.97%

Fig. 5 shows that regions of G02 in which the intermediate conductive layer is well developed primarily support the three-layer model. As the conductor thins toward pinch-out, support shifts toward the two-layer model. Support varies more strongly along G05: one-, two-, and three-layer models all receive support where the intermediate resistive layer disappears and the interfaces vary most strongly. Support for different layer counts is therefore not spatially uniform along a profile. Imposing one layer count on the full profile would obscure these local differences in model support.

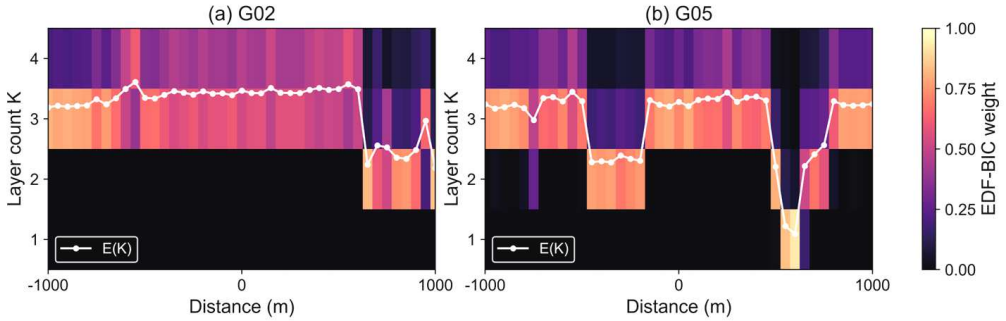


Fig. 5 Station-scale EDF-BIC weights and weighted mean candidate layer counts for G02 and G05

3.4 Comparison of LCMA with fixed-dimension and maximum-support models

Fig. 6 compares three treatments of layer count: a fixed K = 3 model, the stationwise maximum-support model, and LCMA. In G02, the fixed K = 3 model imposes a three-layer parameterization at every station. Where the intermediate conductor shown in Fig. 2b has pinched out, the inversion can approximate the two-layer structure only by reducing the thickness of the intermediate layer or its resistivity contrast with adjacent layers (Fig. 6a). The stationwise maximum-support model retains only the candidate with the largest EDF-BIC weight at each station. This discrete choice can create local discontinuities where the maximum-support layer count changes (Fig. 6b). LCMA instead combines the candidates on a common depth grid using their complete EDF-BIC weight distributions (Fig. 6c). For the reference noise realization, the log-resistivity root-mean-square errors (RMSEs) of the three recovered models are approximately 0.105, 0.111, and 0.100, respectively.

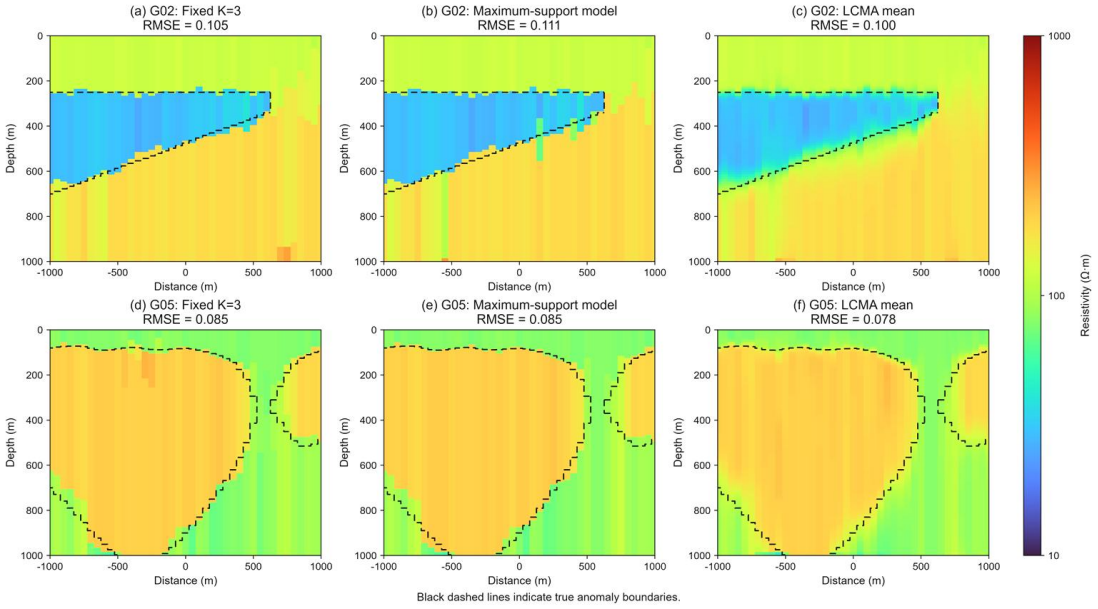


Fig. 6 Effects of three treatments of layer count on structural recovery for G02 and G05. (a-c) Fixed three-layer model, stationwise maximum-EDF-BIC-weight model, and LCMA mean model for G02. (d-f) Corresponding results for G05

In G05, support for the candidate layer counts varies more strongly because the intermediate layer disappears over part of the profile. The log-resistivity RMSEs of the three recovered models are approximately 0.085, 0.085, and 0.078, respectively. Across G02 and G05, LCMA recovers the principal resistivity structures while retaining information from multiple supported layer counts and avoiding conversion of a continuous support distribution into a single layer count at each station. For these two reference noise realizations, LCMA yields the lowest RMSE among the three approaches.

3.5 Decomposition of within- and between-model uncertainty

Using the variance decomposition described in Section 2.4, Fig. 7 compares the spatial distributions of within-model, between-model, and total uncertainty for G02 and G05. The between-model component characterizes structural differences among the supported candidate layer counts.

In G02, between-model uncertainty increases along the progressively thinning conductive layer toward the pinch-out zone. Its maxima broadly coincide with the region in Fig. 5 where support shifts from the three-layer to the two-layer model. In G05, between-model uncertainty is concentrated where the intermediate layer disappears or reappears and where interface variations are strongest (Fig. 7e). Within-model uncertainty, by contrast, varies more continuously in space for a specified layer count (Fig. 7a and 7d). Where candidates recover similar principal resistivity structures, between-model uncertainty is small and total uncertainty is dominated by the within-model component. Where candidates differ in interface presence, interface depth, or local layer count, the between-model component increases, indicating greater sensitivity to layer-count choice.

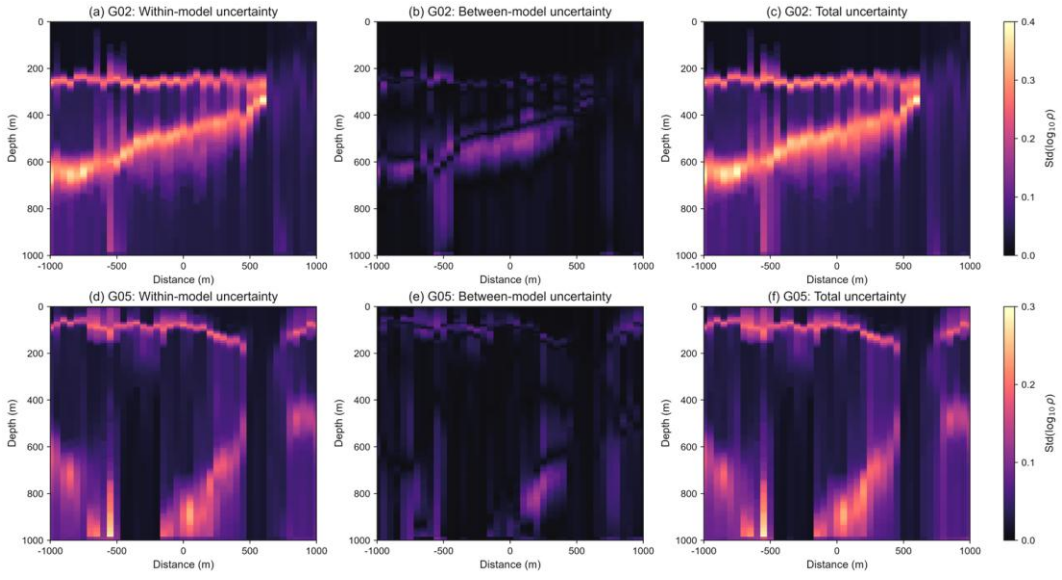


Fig. 7 Model-averaged uncertainty for G02 and G05. (a-c) Within-model parameter uncertainty, between-model layer-count uncertainty, and total uncertainty for G02. (d-f) Corresponding results for G05

3.6 Stability and empirical coverage under repeated noise realizations

To evaluate sensitivity to random noise, 50 independent noise-realization experiments are performed for both G02 and G05. Each realization uses the candidate set, error-weighting scheme, and regularization settings established in the reference experiment; only the observational noise is regenerated. Fig. 8 compares the log-resistivity RMSE, empirical coverage of the P10–P90 interval, and mean interval width for fixed K = 3, nominal-BIC LCMA, the stationwise maximum-support model, and EDF-BIC LCMA. Nominal-BIC LCMA uses the same averaging procedure as EDF-BIC LCMA but derives its weights from nominal BIC. RMSE and mean interval width are calculated in log10-resistivity space, whereas empirical coverage is the proportion of the true resistivity model contained within the P10–P90 interval.

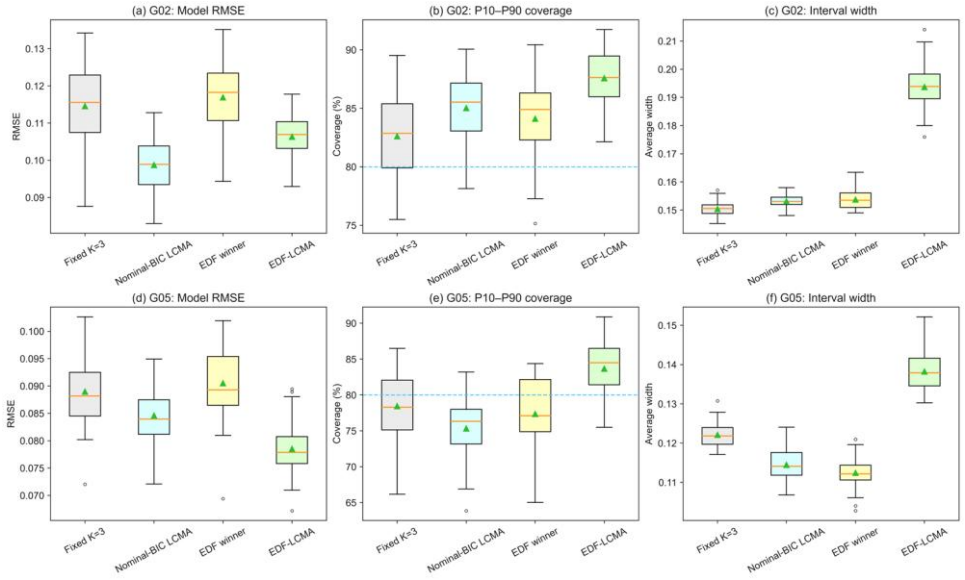


Fig. 8 Statistics from 50 independent noise realizations for G02 and G05. (a-c) Distributions of model RMSE, P10–P90 coverage, and interval width for G02. (d-f) Corresponding results for G05. Boxes span the interquartile range; orange lines mark medians, green triangles mark means, whiskers reach the most extreme values within 1.5 times the interquartile range, and dots mark outliers.

Across the 50 realizations, the model-recovery and uncertainty statistics of EDF-BIC LCMA remain tightly distributed. Values are reported as the mean ± standard deviation. For G02, the RMSE, empirical P10–P90 coverage, and mean interval width are 0.1063 ± 0.0058, 87.57 ± 2.34%, and 0.1937 ± 0.0074, respectively (Fig. 8a–c). The corresponding values for G05 are 0.07850 ± 0.00449, 83.66 ± 3.95%, and 0.13823 ± 0.00477 (Fig. 8d–f). Mean coverage exceeds the nominal 80% level for both models, while RMSE and interval width vary little among realizations. Relative to the other approaches, EDF-BIC LCMA generally provides higher empirical coverage together with wider intervals; coverage should therefore be evaluated jointly with interval width. Under the tested noise model, candidate set, and regularization, the results are stable and are not unduly sensitive to an individual noise realization.

4 Application to the Yemaquan FDEM field data

4.1 Survey setting, data, and geological background

The field data are from grounded-wire-source FDEM profiles L52 and L53 over the Yemaquan Fe-Pb-Zn skarn polymetallic deposit in the western segment of the East Kunlun orogenic belt. The deposit is principally hosted along the contact between Late Triassic intermediate-felsic intrusive rocks and carbonate rocks, where intrusion, metasomatic alteration, and skarn mineralization have produced marked lithological and electrical contrasts (Liu et al., 2013; Zhang et al., 2016). Zhou et al. (2025) previously inverted and interpreted the same data set. Other electromagnetic studies at Yemaquan include frequency-domain subtle-field analysis (Ma et al., 2025), transient-response sign-reversal analysis (Wei et al., 2026), and integrated magnetic and transient electromagnetic interpretation (Beshr et al., 2025). The original survey used an approximately 2.5-km-long grounded-wire source and comprised 112 stations on the two profiles, with a station spacing of approximately 40 m and 30 frequencies from 0.25 to 5120 Hz. Fig. 9 shows the regional location, simplified geological setting, and FDEM survey layout.

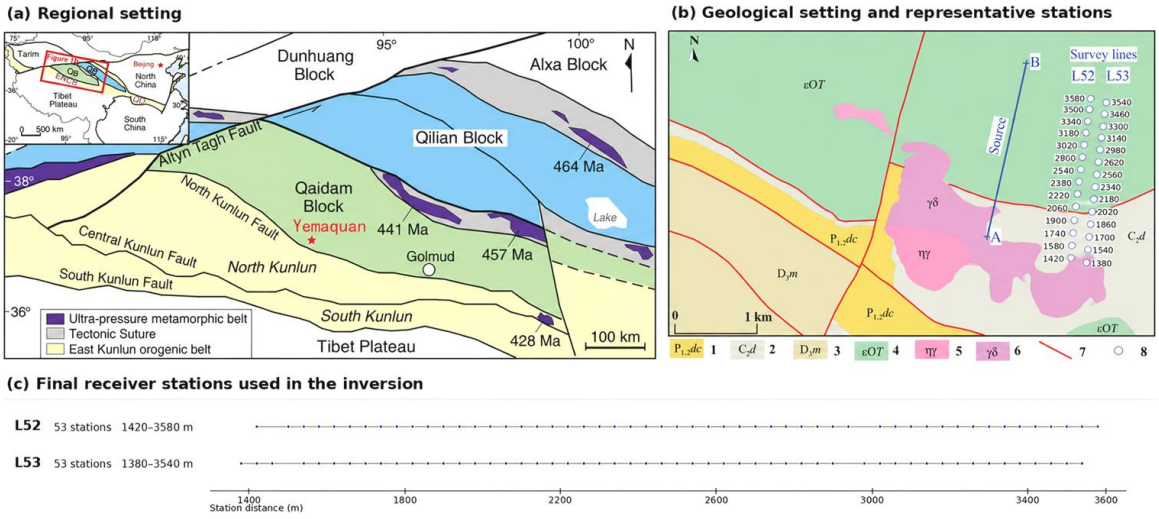


Fig. 9 Location, simplified geological setting, and FDEM survey layout of the Yemaquan deposit. (a) Regional tectonic setting. (b) Simplified geology of the survey area and representative receiver stations. (c) All receiver stations retained for inversion after quality control. Regional tectonics and survey-area geology are modified from Zhou et al. (2025)

The observations retained after quality control for L52 and L53 are shown in Fig. 10 as the amplitude and phase of the complex Ex/Hy response; white regions denote data excluded from the inversion. Each profile retains 53 stations and 29 frequencies from 0.25 to 3840 Hz. L52 and L53 contain 1504 and 1534 valid complex observations, respectively, corresponding to 3008 and 3068 real-valued data components. Data errors are represented by observation-specific standard deviations of the real and imaginary components, subject to minimum errors propagated from the field-ratio uncertainty. Minimum relative amplitude errors of 5% and minimum phase errors of 2 degrees are assigned independently to both Ex and Hy. Propagation in quadrature to the complex Ex/Hy ratio gives minimum amplitude and phase errors of 7.1% and 2.83 degrees, respectively. The final standard deviations of the real and imaginary components

are no smaller than the component errors obtained by first-order propagation of these amplitude and phase minima. Missing data are not interpolated. Forward calculations use the actual source and receiver positions, and the maximum depth of inversion interpretation is 1000 m.

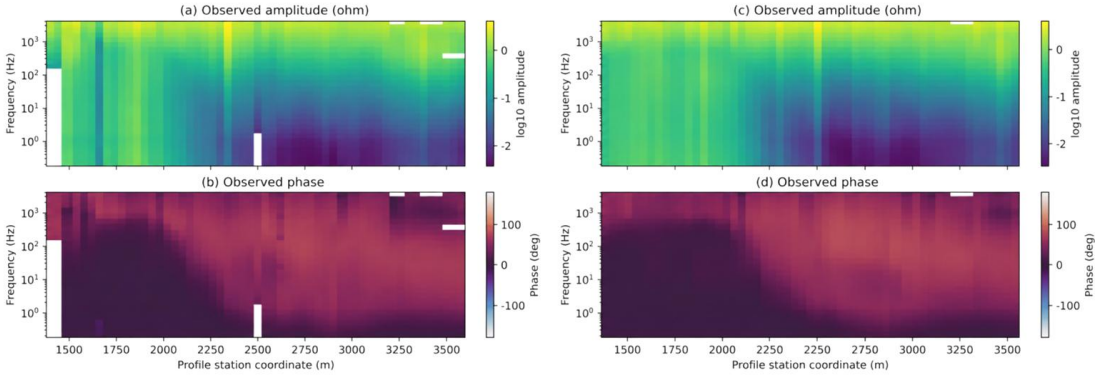


Fig. 10 Observed FDEM data for lines L52 and L53 at Yemaquan. (a-b) Amplitude and phase of the Ex/Hy response along L52. (c-d) Corresponding results for L53. White regions indicate data excluded from the inversion after quality control

Petrophysical measurements, borehole information, and previous inversion results are used only for geological interpretation and comparison and do not enter the objective function. Zhou et al. (2025) reported mean resistivities of approximately 1420, 1057, and 719 Ω·m for granodiorite, marble, and limestone, respectively, and approximately 48 Ω·m for carbonaceous limestone. Various types of magnetite and Pb-Zn-related ores have resistivities of approximately 10–179 Ω·m. Because the resistivity ranges of carbonaceous rocks and some ores overlap substantially, a conductive anomaly alone is not a unique indicator of mineralization. The Occam inversion of Zhou et al. (2025) shows a pronounced resistive-to-conductive transition at approximately 2200–2600 m along L52 and a similar principal lateral electrical zonation along L53, providing an independent structural reference for interpreting the model-averaged results.

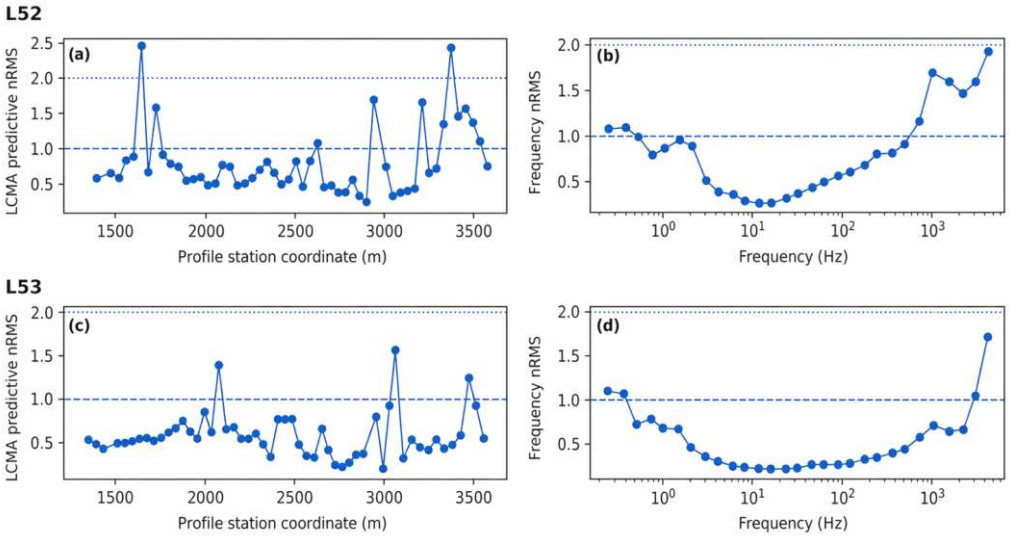


Fig. 11 Fits to the Yemaquan field data. (a-b) Station- and frequency-dependent fits for L52. (c-d) Corresponding results for L53

4.2 Data fit, expansion of candidate layer counts, and computational cost

The model-averaged predicted responses for L52 and L53 show no systematic misfit across an entire profile or broad frequency band (Fig. 11), with overall nRMS values of 0.812 and 0.609, respectively. Most stationwise nRMS values are near or below one; two stations on L52 exceed two, whereas high-residual stations are less common on L53. Residuals increase to some extent at the high-frequency end of both profiles, particularly on L52. The principal features of both data sets are reproduced, so subsequent differences in model support primarily represent relative support among candidate layer counts rather than systematic data misfit.

Table 3. Computational costs of the production runs for G02, G05, L52, and L53. Forward-evaluation counts are stationwise FDEM evaluations recorded in the program logs.

Data set	No. of stations	Candidate K	$\sum \boldsymbol{n_{fev}}/\sum \boldsymbol{n_{jev}}$	Stationwise forward evaluations	Candidate-inversion time	EDF/UQ (s)	Additional cost (%)
G02	41	1–4/8	96/89	22,181	721.3 s	0.276/4.725	0.69
G05	41	1–4/8	93/76	19,803	664.5 s	0.354/5.175	0.83
L52	53	1–8/20	271/224	120,310	4396.9 s	2.719/26.459	0.66
L53	53	1–8/20	268/232	124,656	4541.0 s	2.795/31.620	0.76

The maximum candidate layer count is set to K_{max}=20. Under the common 2% adaptive stopping criterion, expansion stops after K=8 has been evaluated for both L52 and L53. The layer count K describes one parameterization within the finite family of layered candidates. Its EDF-BIC support depends jointly on the error model, regularization, and parameterization and should not be interpreted directly as the number of geological strata.

Table 3 summarizes the computational costs. The candidate-model inversions require approximately 73.3 and 75.7 min for L52 and L53, respectively. EDF calculation and the subsequent uncertainty analysis add only 0.66% and 0.76% to the respective candidate-inversion times. Nonlinear inversion of the different candidate layer counts therefore remains the dominant computational cost for the field data.

4.3 Model support and principal electrical structures

Station-scale EDF-BIC weights show pronounced spatial variation in the relative support among candidate layer counts. The profile-averaged, EDF-BIC-weighted mean candidate layer counts are 6.58 for L52 and 6.08 for L53. At most stations, support is distributed to varying degrees among adjacent layer counts rather than concentrated on one candidate. Applying one uniform layer count or retaining only the stationwise maximum-support candidate would therefore discard part of the support information (Fig. 12d and 12h). The weighted mean layer count summarizes the weight distribution and does not define the layer count of the LCMA result.

Despite local variations in model support, the LCMA results recover relatively robust principal electrical structures. The western part of L52 is dominated by a resistive background and contains a

shallow resistive body between approximately 1700 and 2200 m. Resistivity decreases toward the center of the profile, and the region east of approximately 2400-2500 m is generally more conductive (Fig. 12a). L53 similarly shows a resistive western region and a more conductive central-to-eastern region, although local electrical boundaries and the geometry of deeper extensions differ (Fig. 12e). The LCMA mean and P50 models give consistent representations of these large-scale structures while avoiding the local structural discontinuities that can arise when only the maximum-support model is retained at each station.

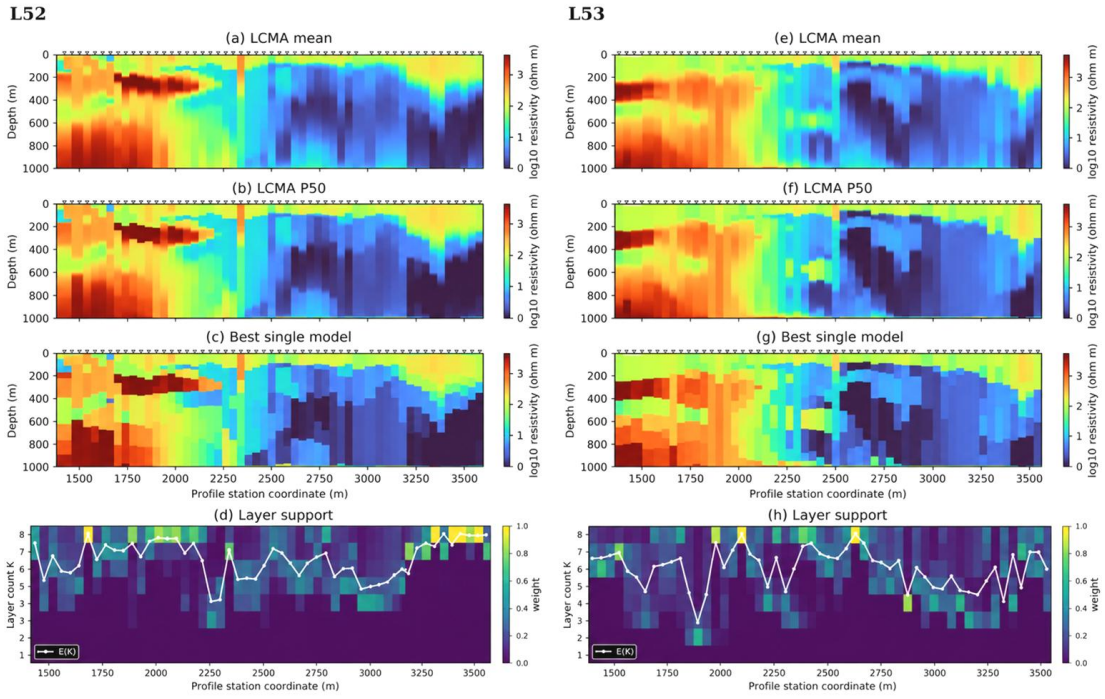


Fig. 12 Recovered resistivity structures and layer-count support for L52 and L53. (a-d) LCMA mean model, LCMA median model, stationwise maximum-support model, and layer-count support for L52. (e-h) Corresponding results for L53

The principal electrical pattern recovered by LCMA is broadly consistent with the Occam inversion of Zhou et al. (2025), particularly the main resistive-to-conductive transition between approximately 2200 and 2600 m along L52 and the similar lateral electrical zonation along L53. Because the two studies use different observables, error treatments, and parameterizations, the earlier results are used only as an independent structural reference; data-fit metrics are not compared directly. Existing petrophysical data indicate that the resistive zones are compatible with intrusive rocks and some carbonate rocks. The regional conductive zones may be associated with carbonaceous carbonate rocks and may also include local responses from conductive mineralization. The mineralization significance of any conductive anomaly therefore requires additional constraints from borehole and geological data.

4.4 Model-averaged uncertainty and robustness of interpretation

For the field data, total model-averaged uncertainty is decomposed into within- and between-model components. Averaged over each profile, the within-model component contributes 89.3% of the variance on L52 and 85.7% on L53 (Fig. 13a and 13d), whereas the between-model component contributes 10.7%

and 14.3%, respectively (Fig. 13b and 13e). Total uncertainty on both profiles is therefore dominated by continuous-parameter uncertainty conditional on a fixed layer count. The between-model component is more spatially concentrated, reaching maximum local fractions of approximately 42.5% on L52 and 40.6% on L53. Layer-count uncertainty is thus not the dominant source of variance at the profile scale but makes a non-negligible local contribution in structural transition zones.

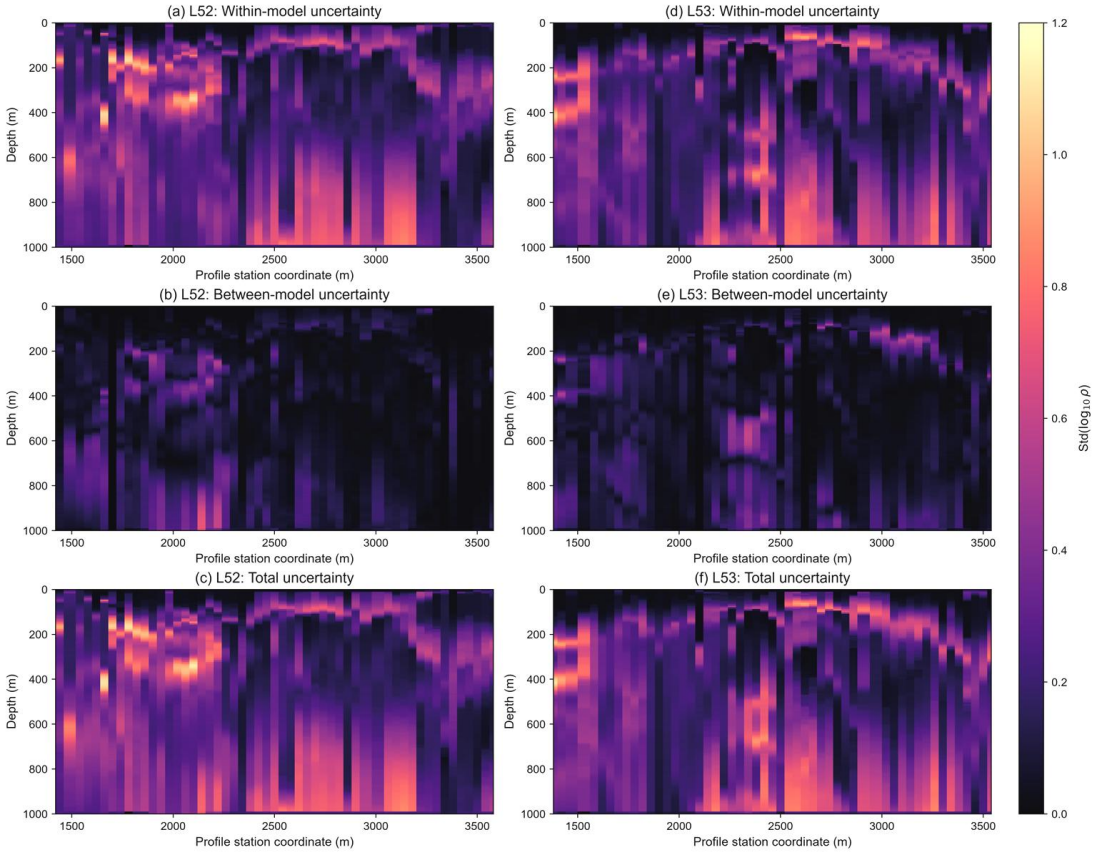


Fig. 13 Model-averaged structural uncertainty for L52 and L53. (a-c) Within-model parameter uncertainty, between-model layer-count uncertainty, and total uncertainty for L52. (d-f) Corresponding results for L53

On L52, elevated between-model uncertainty is concentrated mainly between approximately 1900 and 2260 m, where the western resistive region transitions into the central conductive region, and in intervals where the candidates recover substantially different deep interfaces. The principal resistive and conductive units remain broadly stable in the LCMA result, whereas the corresponding P10–P90 intervals widen across their contact zones. L53 shows a similar pattern: higher between-model uncertainty occurs mainly in the central electrical transition between approximately 2260 and 2340 m and around some deeper interface variations. The principal conductive region from the center to the east is continuous, but its internal subdivision and lower boundary are more uncertain.

Across the two profiles, the principal resistive and conductive zones remain broadly consistent among the supported candidate layer counts and the independent Occam inversion. Local interface positions, deep extensions, and fine-scale geometries are more sensitive to layer count. This contrast helps distinguish

relatively robust large-scale electrical structure from local features that depend more strongly on the selected layer count.

5 Discussion

5.1 Model complexity and dimension support in regularized inversion

Appropriate characterization of model complexity is fundamental when information criteria are used to assess candidate layer counts in regularized inversion. For layered FDEM inversion, the parameter space expands with layer count, but added resistivity and thickness parameters do not translate proportionally into independent data-fitting capacity. Limited data sensitivity, parameter correlation, and regularization reduce the contribution of some additional parameters to the fit, creating a potentially substantial difference between nominal parameter count and effective model complexity. The contrasting support obtained from nominal BIC and EDF-BIC for the same U05 candidate inversions illustrates the consequence of this difference. The EDF adjustment measures complexity using the data-fitting degrees of freedom retained after regularization and thereby provides a more appropriate basis for comparing candidate layer counts.

In addition to modifying the complexity measure, differences in EDF-BIC quantify relative support among a finite set of candidate layer counts. These differences are used to construct the LCMA weights. The weights support relative comparison and model averaging only within the evaluated candidate set and are not interpreted as exact posterior model probabilities.

For laterally constrained profile inversion, support for layer count also has a spatial character. The profile-wide EDF-BIC determines whether adding another candidate layer count continues to improve the balance between fit and complexity across the profile, whereas the station-scale weights describe local relative support within the evaluated set. These quantities govern candidate-set expansion and the spatial distribution of model support, respectively, and therefore do not have identical statistical interpretations. The adaptive stopping rule controls the number of candidates evaluated; it does not impose an absolute layer-count limit at every station. This treatment preserves the profile-wide regularized inversion while allowing local structure and data resolution to influence support along the profile.

5.2 From model selection to model averaging: interpretive implications of dimension uncertainty

Comparisons among a finite set of candidate models commonly culminate in selection of a preferred parameterization, but the existence of a highest-weight candidate does not imply that layer-count uncertainty has vanished. Even where the same layer count receives the largest weight, the concentration of support can vary substantially from one location to another. Retaining only the maximum-support model prevents these differences in parameterization certainty from entering the final interpretation. LCMA preserves the residual differences in candidate support and includes multiple supported models in the final result. Improved continuity may follow from averaging, but it is a consequence rather than the primary

purpose of LCMA. The method represents both the preferred candidate and the strength of its support relative to the alternatives, avoiding reduction of layer-count assessment to a single discrete choice.

A model-averaged resistivity structure must also be distinguished from any fixed-layer-count model. After candidates are mapped to a common depth grid, LCMA represents a weighted average over supported parameterizations rather than a new discrete geological model with a defined layer count and number of interfaces. LCMA is therefore best suited to identifying the principal resistive and conductive units recovered consistently across layer counts. Features that depend more strongly on parameterization, including interface existence, interface depth, and local layer count, must be interpreted jointly with the candidate-support distribution and between-model uncertainty. This distinction is particularly important near pinch-outs, disappearing layers, and strong interface variations, where several layer counts can provide different but similarly acceptable structures at comparable levels of data fit.

The within- and between-model variance decomposition reveals the source, rather than only the magnitude, of total uncertainty. When the within-model component dominates and the between-model component is small, the candidate layer counts provide broadly consistent representations of the principal structures; most uncertainty then arises from limited resolution of resistivity, layer thickness, or interface position within a fixed parameterization. An increase in the between-model component indicates that different supported layer counts yield more divergent local structural interpretations. Although between-model uncertainty enters total variance additively, it also measures the sensitivity of structural interpretation to layer-count choice. Structural uncertainty has previously been quantified to assess confidence in electromagnetic inversion (Minsley et al., 2021); the between-model component used here is specifically the contribution arising from the evaluated candidate layer counts.

The spatial concentration of layer-count uncertainty can be understood as an expression of increased equivalence among parameterizations near structural transitions (Grayver and Kuvshinov, 2016). Candidate models can retain or merge a thin layer, or shift interface positions, to produce different structural representations with similar data fits. Where multiple layer counts consistently recover the principal electrical units, the between-model component is generally small. Its importance should therefore not be judged solely from its profile-wide mean contribution: even when that contribution is modest, local maxima may identify locations most sensitive to interpretation.

The repeated-noise experiments provide an empirical test of the stability of model recovery and UQ under random perturbations. With the candidate set, data-error model, and regularization fixed, model-recovery error, empirical coverage, and interval width remain broadly stable across noise realizations. Coverage must nevertheless be considered together with interval width, because greater coverage obtained solely by widening the interval does not necessarily indicate an improved uncertainty estimate (Gneiting et al., 2007).

5.3 Methodological scope, computational characteristics, and applicability

This study addresses the same broad problem of model-dimension uncertainty as trans-dimensional Bayesian inversion but follows a different inferential route. Trans-dimensional Bayesian methods sample

the joint model space and explore model dimension and continuous parameters simultaneously (Green, 1995; Malinverno, 2000, 2002; Sambridge et al., 2006). Recent geophysical UQ studies have also sought to reduce computational cost through efficient Bayesian sampling, variational approximations, and randomized regularization (Minson, 2024; Wu et al., 2025; Vargas Huitzil et al., 2025). In contrast to methods that explore a posterior distribution directly or construct randomized model ensembles, the finite-candidate approach used here evaluates relative support among layer counts after conventional regularized inversion and combines LCMA with a local, fixed-layer-count Laplace approximation. The result is a model-averaged UQ framework built on deterministic candidate inversions that integrates directly with existing workflows while retaining layer-count differences in the final result.

The main computational cost remains the nonlinear inversion of the candidate layer counts. Once a candidate has been inverted, the Jacobian and Gauss-Newton Hessian at the final solution can be reused for both EDF and local candidate-conditional uncertainty estimation. Model support, LCMA, and subsequent UQ therefore add only modest post-processing costs. Total cost is governed primarily by the number of candidate layer counts evaluated. Reusing local linear information from the deterministic inversions avoids a separate large-scale posterior-sampling procedure for model averaging and candidate-conditional UQ.

The uncertainties reported here must be interpreted conditionally on the candidate set, data-error model, and regularization. The fixed-dimensional Laplace approximation primarily describes local parameter uncertainty near the final regularized solution, whereas the between-model component captures only the model-dimension uncertainty caused by variation in the evaluated layer counts. It does not include uncertainty in the regularization parameters, error model, or more general model classes. Applying a common error model and regularization setup to all dimensions focuses the comparison on changes in dimension, so the present results are conditional on those choices. In addition, the current implementation caps conditional standard deviations in weakly constrained directions to suppress extreme variances under the local Gaussian approximation; this numerical truncation may affect the estimated uncertainty magnitude along the least constrained parameter directions. Previous Bayesian electromagnetic inversion studies have shown that nonlinearity can substantially alter posterior structure (Guo et al., 2011). More complete probabilistic sampling may therefore provide additional information when the fixed-dimensional posterior is strongly non-Gaussian, multimodal, or nonlinear. Extension to 2D or 3D parameterizations or to a broader candidate space will require comparable EDF calculations across parameterizations and a common representation in which to express the resulting models.

Neither EDF-BIC nor LCMA is intrinsically tied to a particular FDEM profile or form of lateral constraint. In principle, if candidate parameterizations can be inverted under a common error model and the corresponding data Jacobian and regularization curvature are available, their effective fitting degrees of freedom can be evaluated and used for model averaging. Extension to more complex model spaces will depend on maintaining comparable complexity measures across parameterizations and establishing a consistent representation for model averaging and uncertainty quantification.

6 Conclusions

An EDF-BIC framework has been introduced for layer-count assessment and LCMA-based uncertainty quantification in FDEM inversion. EDF-BIC replaces the nominal parameter count with the data-fitting degrees of freedom retained after regularization and converts criterion differences among candidate layer counts into relative-support weights. LCMA uses these weights to combine multiple supported candidates and decomposes total model-averaged uncertainty into within- and between-model components.

The U05 synthetic experiment shows that the EDF adjustment reduces the low-layer-count preference of nominal BIC for the regularized five-layer reference model. In the laterally varying G02 and G05 experiments, EDF-BIC support shifts spatially near layer pinch-outs, disappearing layers, and interface variations; between-model uncertainty is concentrated where candidate layer counts produce different structural representations. Across 50 independent noise realizations, mean empirical coverage of the P10–P90 interval is 87.57% for G02 and 83.66% for G05, while model-recovery errors and interval widths remain stable. The Yemaquan L52 and L53 results further indicate that principal resistive and conductive structures reproduced across candidate layer counts are relatively robust, whereas local interfaces and deep extensions are more sensitive to layer-count choice.

The method can be implemented from a finite set of conventional deterministic FDEM inversions. EDF calculation and model-averaged uncertainty analysis reuse the Jacobian and Gauss-Newton Hessian and add less than 1% to the candidate-inversion time in the reported experiments. No separate full posterior-sampling procedure is required. The framework therefore provides a computationally tractable approach to layer-count assessment and propagation of the associated uncertainty in regularized FDEM inversion.

Acknowledgments

This work was financially supported by Deep Earth Probe and Mineral Resources Exploration-National Science and Technology Major Project (2024ZD1002905), National Natural Science Foundation of China (42474187), and the Strategic Priority Research Program of the Chinese Academy of Sciences (grant no. XDA0430203).

References

Auken, E. & Christiansen, A.V., 2004. Layered and laterally constrained 2D inversion of resistivity data. Geophysics, 69(3), 752–761. https://doi.org/10.1190/1.1759461.

Auken, E., Christiansen, A.V., Jacobsen, B.H., Foged, N. & Sørensen, K.I., 2005. Piecewise 1D laterally constrained inversion of resistivity data. Geophysical Prospecting, 53(4), 497–506. https://doi.org/10.1111/j.1365-2478.2005.00486.x.

Beshr, A.M., Li, H., Hussain, M. & Memon, F.A., 2025. Inversion of magnetic and transient electromagnetic data for the characterization of skarn polymetallic mineralization in the Qimantagh Metallogenic Belt, China. Ore Geology Reviews, 186, 106902. https://doi.org/10.1016/j.oregeorev.2025.106902.

Blatter, D., Key, K., Ray, A., Foley, N., Tulaczyk, S. & Auken, E., 2018. Trans-dimensional Bayesian inversion of airborne transient EM data from Taylor Glacier, Antarctica. Geophysical Journal International, 214(3), 1919–1936. https://doi.org/10.1093/gji/ggy255.

Blatter, D., Morzfeld, M., Key, K. & Constable, S., 2022a. Uncertainty quantification for regularized inversion of electromagnetic geophysical data—Part I: Motivation and theory. Geophysical Journal International, 231(2), 1057–1074. https://doi.org/10.1093/gji/ggac241.

Blatter, D., Morzfeld, M., Key, K. & Constable, S., 2022b. Uncertainty quantification for regularized inversion of electromagnetic geophysical data—Part II: Application in 1-D and 2-D problems. Geophysical Journal International, 231(2), 1075–1095. https://doi.org/10.1093/gji/ggac242.

Branch, M.A., Coleman, T.F. & Li, Y., 1999. A subspace, interior, and conjugate gradient method for large-scale bound-constrained minimization problems. SIAM Journal on Scientific Computing, 21(1), 1–23. https://doi.org/10.1137/S1064827595289108.

Buckland, S.T., Burnham, K.P. & Augustin, N.H., 1997. Model selection: An integral part of inference. Biometrics, 53(2), 603–618. https://doi.org/10.2307/2533961.

Burnham, K.P. & Anderson, D.R., 2004. Multimodel inference: Understanding AIC and BIC in model selection. Sociological Methods & Research, 33(2), 261–304. https://doi.org/10.1177/0049124104268644.

Constable, S.C., Parker, R.L. & Constable, C.G., 1987. Occam's inversion: A practical algorithm for generating smooth models from electromagnetic sounding data. Geophysics, 52(3), 289–300. https://doi.org/10.1190/1.1442303.

Craven, P. & Wahba, G., 1979. Smoothing noisy data with spline functions: Estimating the correct degree of smoothing by the method of generalized cross-validation. Numerische Mathematik, 31(4), 377–403. https://doi.org/10.1007/BF01404567.

Di, Q.Y., Xue, G.Q., Fu, C.M. & Wang, R., 2020. An alternative tool to controlled-source audio-frequency magnetotellurics method for prospecting deeply buried ore deposits. Science Bulletin, 65(8), 611–615. https://doi.org/10.1016/j.scib.2020.02.007.

Draper, D., 1995. Assessment and propagation of model uncertainty. Journal of the Royal Statistical Society: Series B, 57(1), 45–70. https://doi.org/10.1111/j.2517-6161.1995.tb02015.x.

Farquharson, C.G. & Oldenburg, D.W., 1998. Non-linear inversion using general measures of data misfit and model structure. Geophysical Journal International, 134(1), 213–227. https://doi.org/10.1046/j.1365-246x.1998.00555.x.

Fong, D.C.-L. & Saunders, M., 2011. LSMR: An iterative algorithm for sparse least-squares problems. SIAM Journal on Scientific Computing, 33(5), 2950–2971. https://doi.org/10.1137/10079687X.

Gehrmann, R.A.S., Schwalenberg, K., Riedel, M., Spence, G.D., Spieß, V. & Dosso, S.E., 2016. Bayesian inversion of marine controlled source electromagnetic data offshore Vancouver Island, Canada. Geophysical Journal International, 204(1), 21–38.

Gneiting, T., Balabdaoui, F. & Raftery, A.E., 2007. Probabilistic forecasts, calibration and sharpness. Journal of the Royal Statistical Society: Series B, 69(2), 243–268. https://doi.org/10.1111/j.1467-9868.2007.00587.x.

Grayver, A.V. & Kuvshinov, A.V., 2016. Exploring equivalence domain in nonlinear inverse problems using Covariance Matrix Adaption Evolution Strategy (CMAES) and random sampling. Geophysical Journal International, 205(2), 971–987. https://doi.org/10.1093/gji/ggw063.

Green, P.J., 1995. Reversible jump Markov chain Monte Carlo computation and Bayesian model determination. Biometrika, 82(4), 711–732. https://doi.org/10.1093/biomet/82.4.711.

Guo, R., Dosso, S.E., Liu, J., Dettmer, J. & Tong, X., 2011. Non-linearity in Bayesian 1-D magnetotelluric inversion. Geophysical Journal International, 185(2), 663–675. https://doi.org/10.1111/j.1365-246X.2011.04996.x.

Guo, Z.W., Xue, G.Q., Liu, J.X. & Wu, X., 2020. Electromagnetic methods for mineral exploration in China: A review. Ore Geology Reviews, 118, 103357. https://doi.org/10.1016/j.oregeorev.2020.103357.

Hoeting, J.A., Madigan, D., Raftery, A.E. & Volinsky, C.T., 1999. Bayesian model averaging: A tutorial. Statistical Science, 14(4), 382–417. https://doi.org/10.1214/ss/1009212519.

Konishi, S. & Kitagawa, G., 1996. Generalised information criteria in model selection. Biometrika, 83(4), 875–890. https://doi.org/10.1093/biomet/83.4.875.

Liu, J.N., Feng, C.Y., Zhao, Y.M., Li, D.X., Xiao, Y., Zhou, J.H. & Ma, Y.S., 2013. Characteristics of intrusive rock, metasomatites, mineralization and alteration in Yemaquan skarn Fe-Zn polymetallic deposit, Qinghai Province [in Chinese with English abstract]. Mineral Deposits, 32(1), 77–93.

Liu, W.Y., Yin, C.C., Su, Y., Zhang, B., Xue, S.Y., Liu, Y.H. & Ren, X.Y., 2025. Trans-dimensional Bayesian inversion of airborne electromagnetic data based on artificial-neural-network forward modeling [in Chinese with English abstract]. Chinese Journal of Geophysics, 68(8), 2928-2940. https://doi.org/10.6038/cjg2025S0572.

Ma, X., Zhou, N., Wang, Y., Wei, X. & Shi, J., 2025. Analysis of subtle field from frequency-domain electromagnetic response with short-offset grounded-wire sources. IEEE Geoscience and Remote Sensing Letters, 22, 7508005. https://doi.org/10.1109/LGRS.2025.3586926.

MacKay, D.J.C., 1992. Bayesian interpolation. Neural Computation, 4(3), 415–447. https://doi.org/10.1162/neco.1992.4.3.415.

Malinverno, A., 2000. A Bayesian criterion for simplicity in inverse problem parametrization. Geophysical Journal International, 140(2), 267–285. https://doi.org/10.1046/j.1365-246x.2000.00008.x.

Malinverno, A., 2002. Parsimonious Bayesian Markov chain Monte Carlo inversion in a nonlinear geophysical problem. Geophysical Journal International, 151(3), 675–688. https://doi.org/10.1046/j.1365-246X.2002.01847.x.

Minsley, B.J., 2011. A trans-dimensional Bayesian Markov chain Monte Carlo algorithm for model assessment using frequency-domain electromagnetic data. Geophysical Journal International, 187(1), 252–272. https://doi.org/10.1111/j.1365-246X.2011.05165.x.

Minsley, B.J., Foks, N.L. & Bedrosian, P.A., 2021. Quantifying model structural uncertainty using airborne electromagnetic data. Geophysical Journal International, 224(1), 590–607. https://doi.org/10.1093/gji/ggaa393.

Minson, S.E., 2024. Cross-fade sampling: Extremely efficient Bayesian inversion for a variety of geophysical problems. Geophysical Journal International, 239(3), 1629–1649. https://doi.org/10.1093/gji/ggae353.

Mitsuhata, Y., Uchida, T. & Amano, H., 2002. 2.5-D inversion of frequency-domain electromagnetic data generated by a grounded-wire source. Geophysics, 67(6), 1753–1768.

Ray, A. & Key, K., 2012. Bayesian inversion of marine CSEM data with a trans-dimensional self-parametrizing algorithm. Geophysical Journal International, 191(3), 1135–1151. https://doi.org/10.1111/j.1365-246X.2012.05677.x.

Sambridge, M., Gallagher, K., Jackson, A. & Rickwood, P., 2006. Trans-dimensional inverse problems, model comparison and the evidence. Geophysical Journal International, 167(2), 528–542. https://doi.org/10.1111/j.1365-246X.2006.03155.x.

Schwarz, G., 1978. Estimating the dimension of a model. The Annals of Statistics, 6(2), 461–464. https://doi.org/10.1214/aos/1176344136.

Tierney, L. & Kadane, J.B., 1986. Accurate approximations for posterior moments and marginal densities. Journal of the American Statistical Association, 81(393), 82–86. https://doi.org/10.1080/01621459.1986.10478240.

Vargas Huitzil, E., Morzfeld, M. & Constable, S., 2025. RamBO: randomized blocky Occam, a practical algorithm for generating blocky models and associated uncertainties. Geophysical Journal International, 241(1), 567–579. https://doi.org/10.1093/gji/ggaf055.

Viezzoli, A., Christiansen, A.V., Auken, E. & Sørensen, K., 2008. Quasi-3-D modeling of airborne TEM data by spatially constrained inversion. Geophysics, 73(3), F105–F113. https://doi.org/10.1190/1.2895521.

Wei, X., Zhou, N. & Zhang, Z., 2026. Analysis of the sign reversal phenomena in grounded-wire transient electromagnetic response—A case study of the Yemaquan skarn-type iron polymetallic deposit. Journal of Applied Geophysics, 244, 106024. https://doi.org/10.1016/j.jappgeo.2025.106024.

Werthmüller, D., 2017. An open-source full 3D electromagnetic modeler for 1D VTI media in Python: empymod. Geophysics, 82(6), WB9–WB19. https://doi.org/10.1190/GEO2016-0626.1.

Wu, S., Sun, J. & Chen, J., 2025. Variational inference for geophysical Bayesian inverse problems using normalizing flows: An unsupervised approach to electromagnetic data inversion. Geophysical Journal International, 242(3), ggaf239. https://doi.org/10.1093/gji/ggaf239.

Xiang, E., Guo, R., Dosso, S.E., Liu, J., Dong, H. & Ren, Z., 2018. Efficient hierarchical trans-dimensional Bayesian inversion of magnetotelluric data. Geophysical Journal International, 213(3), 1751–1767. https://doi.org/10.1093/gji/ggy071.

Ye, J., 1998. On measuring and correcting the effects of data mining and model selection. Journal of the American Statistical Association, 93(441), 120–131. https://doi.org/10.1080/01621459.1998.10474094.

Zhang, A.K., Mo, X.X., Yuan, W.M., Liu, G.L., Zhu, C.B. & Hao, N.N., 2016. Petrogensis and tectonic setting of Yemaquan Triassic granite from the West of the Eastern Kunlun Mountain Range, China [in Chinese with English abstract]. Acta Mineralogica Sinica, 36, 157–173.

Zhou, N.N., Wei, X.H. & Zhang, Z.H., 2025. Electromagnetic evidence of the shielding effect of carbonaceous rocks in the skarn-type iron-lead-zinc polymetallic mineralization: A case study of the Yemaquan deposit in the East Kunlun orogenic belt. Geophysics, 90(4), B171–B181. https://doi.org/10.1190/GEO2024-0341.1.